

Study of neoclassical transport and bootstrap current for W7-X in the $1/\nu$ regime, using results from the PIES code

V V Nemov¹, V N Kalyuzhnyj¹, S V Kasilov¹, M Drevlak²,
J Nührenberg², W Kernbichler³, A Reiman⁴ and D Monticello⁴

¹ Institute of Plasma Physics, National Science Center 'Kharkov Institute of Physics and Technology', Akademicheskaya str. 1, 61108 Kharkov, Ukraine

² Max-Planck-Institute für Plasmaphysik, Teilinstitut Greifswald IPP-EURATOM Association, D-17491 Greifswald, Germany

³ Institut für Theoretische Physik, Technische Universität Graz, Petersgasse 16, A-8010 Graz, Austria

⁴ Princeton Plasma Physics Laboratory, Princeton, NJ 08543, USA

Received 4 July 2003

Published 26 November 2003

Online at stacks.iop.org/PPCF/46/179 (DOI: 10.1088/0741-3335/46/1/011)

Abstract

For the magnetic field of the Wendelstein 7-X (W7-X) standard high-mirror configuration, computed by the PIES code, taking into account real coil geometry, neoclassical transport and bootstrap current are analysed in the $1/\nu$ regime using methods based on the integration along magnetic field lines in a given magnetic field. The zero β and $\langle\beta\rangle = 1\%$ cases are studied. The results are compared to the corresponding results for the vacuum magnetic field directly produced by modular coils. A significant advantage of W7-X over a conventional stellarator resulting from reduced neoclassical transport and from reduced bootstrap current follows from the computations although the neoclassical transport is somewhat larger than that previously obtained for the ideal W7-X model configuration.

1. Introduction

An important part of stellarator optimization is related to the use of computations from the PIES code. The PIES code [1] is a three-dimensional finite beta equilibrium code which is widely used for stellarator plasma equilibrium computations (e.g. [2]) taking into account a finite plasma pressure as well as external currents. This code was developed without the *a priori* assumption of nested magnetic surfaces. The magnetic field obtained as a result of the PIES code is presented in real space coordinates and can be used for an investigation of the stellarator confinement properties in real space coordinates taking into account both the finite plasma beta and the direct influence of coil currents.

In this paper, the magnetic field data obtained as a result of the PIES code for the Wendelstein 7-X (W7-X) configuration [3, 4] are used for calculations of neoclassical transport and bootstrap currents in the $1/\nu$ regime.

For these calculations, the techniques [5–7] of the $1/\nu$ transport and bootstrap current calculations are used, which are based on the integration along magnetic field lines in a given magnetic field. One of the characteristic features of these techniques is that if the magnetic field is originally available in real-space coordinates, calculations can be performed without a field transformation to magnetic coordinates. The case considered here corresponds to the free boundary equilibrium with $\langle\beta\rangle = 1\%$. For comparison, the zero β case is also considered using both the PIES output and the data for the currents in modular coils.

Note that the neoclassical transport properties and bootstrap currents for W7-X, which is an optimized stellarator of the Helias-type [8], have been already studied in the design phase of this device with the DKES code and with the Monte-Carlo technique (see, e.g. [4, 9]). The results obtained in this paper are useful in extending our knowledge of W7-X confinement properties.

This paper is arranged as follows. In section 2 the representation of the magnetic field is discussed. The computation of the neoclassical transport is carried out in sections 3 and 4. Section 5 is devoted to the bootstrap current computations. To clarify some issues related to neoclassical transport, the second adiabatic invariant is analysed in section 6 for the $\langle\beta\rangle = 1\%$ case. A short discussion of all results is given in section 7.

2. Magnetic field representation and magnetic configurations

In cylindrical coordinates, R , φ , z , the magnetic field calculated by the PIES code can be represented in the following form:

$$B_R = \sum_{m=0}^{m_{\max}} \sum_{n=-n_{\max}}^{n_{\max}} B_{R,m,n}(s) \sin(nn_p\varphi - m\theta), \quad (1)$$

$$B_z = \sum_{m=0}^{m_{\max}} \sum_{n=-n_{\max}}^{n_{\max}} B_{z,m,n}(s) \cos(nn_p\varphi - m\theta), \quad (2)$$

$$B_\varphi = R \sum_{m=0}^{m_{\max}} \sum_{n=-n_{\max}}^{n_{\max}} B_{m,n}^\varphi(s) \cos(nn_p\varphi - m\theta), \quad (3)$$

$$R = \sum_{m=0}^{m_{\max}} \sum_{n=-n_{\max}}^{n_{\max}} R_{m,n}(s) \cos(nn_p\varphi - m\theta), \quad (4)$$

$$z = \sum_{m=0}^{m_{\max}} \sum_{n=-n_{\max}}^{n_{\max}} z_{m,n}(s) \sin(nn_p\varphi - m\theta). \quad (5)$$

Here, s , θ and φ specify the background coordinate system in which all the quantities calculated by the PIES code are determined and n_p is the number of field periods (for W7-X $n_p = 5$). The coordinates s , θ and φ are real space coordinates. In contrast to magnetic coordinates, the s value is not constant on a magnetic surface. The decomposition coefficients $B_{R,m,n}$, $B_{z,m,n}$, $B_{m,n}^\varphi$, $R_{m,n}$ and $z_{m,n}$ of the spectra (1)–(5) are given in sets of data obtained as results of a PIES run. The radial dependences of these coefficients are given for a set of discrete radial mesh points $s_j = j/j_{\max}$, $j = 1, 2, \dots, j_{\max}$. Between the mesh points, the decomposition coefficients are found using splines. The use of splines is also necessary to calculate the

magnetic field spatial derivatives. For the $\beta = 0$ case $m_{\max} = 18$, $n_{\max} = 16$ and $j_{\max} = 80$, and for the $(\beta) = 1\%$ case $m_{\max} = 20$, $n_{\max} = 18$ and $j_{\max} = 100$.

The W7-X standard high mirror configuration, which is considered in this paper, has the following main parameters: aspect ratio $A = 10.45$; major radius $R_0 = 5.5$ m; number of field periods (along the torus) $n_p = 5$; and total number of modular coils is 50. The optimization properties are determined by a special choice of the modular coil geometry. In the case of the vacuum magnetic field, this field as well as its spatial derivatives are calculated using the Biot–Savart law for the modular coils which are modelled as closed filamentary conductors (each coil by one filament). Each of the coils is split into 96 short, straight conductors.

For the case of the magnetic field produced by modular coils, computations of all quantities considered in this work are performed in cylindrical coordinates. As for the case of the magnetic field from the PIES code, the analogous computations are carried out in the background coordinate system s , θ and φ . In this case, the necessary coordinate vectors as well as the quantities ∇s and $\nabla\theta$ are calculated on the basis of formulae (4) and (5). In particular, the contravariant components of \mathbf{B} , B^s and B^θ , are necessary in this case for the integration of the magnetic field lines. These components can be calculated as $B^s = \mathbf{B} \cdot \nabla s$ and $B^\theta = \mathbf{B} \cdot \nabla\theta$. It is necessary to note that the contravariant components of \mathbf{B} are also obtained directly from the sets of data obtained as a result of a PIES run. In particular, the $B_{m,n}^\varphi(s)$ decomposition coefficients in formula (3) represent the contravariant component B^φ . Using components of \mathbf{B} , magnetic surface computations can be performed. However, for neoclassical transport and bootstrap current computations, spatial derivatives of \mathbf{B} are also needed as it follows from the next sections. These quantities are also calculated from expressions (1)–(5) and included in the corresponding field line tracing codes.

The magnetic surfaces for the vacuum magnetic field produced by the modular coils are shown in figure 1 in the $\varphi = 0$ cross section and after one half of the magnetic field period. Thick lines in the figure separate the inner region from the outer region, where island surfaces with $\iota = 5/5$ are present. These islands and nearby magnetic surfaces are not very close to the modular coils. Therefore, their character and their shapes are insensitive to an increase in the number of segments and filaments modelling each modular coil to values higher than 96 and 1, respectively.

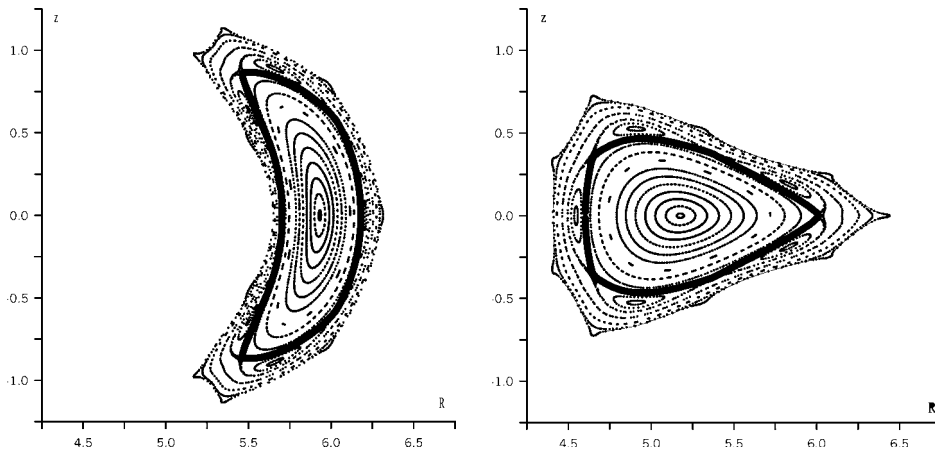


Figure 1. Magnetic surfaces for the vacuum magnetic field produced by modular coils in the $\varphi = 0$ plane (left) and after one half of the magnetic field period (right); thick curves belong to the outermost magnetic surface resulting from a PIES run for the zero β case.

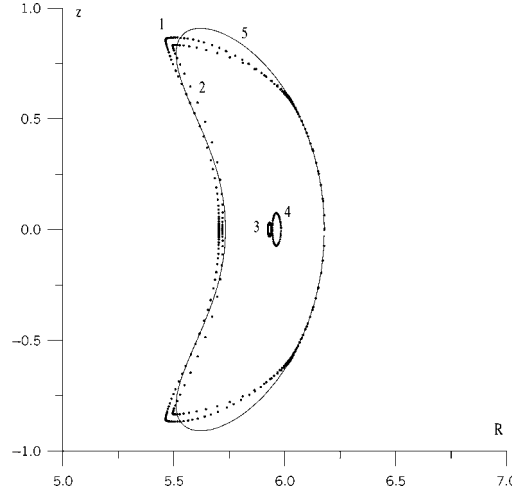


Figure 2. The outermost and inner magnetic surfaces for the magnetic fields obtained as results of PIES runs for $\beta = 0$ (curves 1 and 3) and for $\langle\beta\rangle = 1\%$ (curves 2 and 4). The magnetic surface corresponding to curve 1 practically coincides with the magnetic surface corresponding to thick lines in figure 1. Curve 5 shows the starting boundary surface for the free boundary run in the $\beta = 0$ case.

Figure 2 shows some results for magnetic surfaces obtained as results of PIES runs (in the $\varphi = 0$ plane). Curves 1 and 3 correspond to the outermost and the inner magnetic surfaces for the $\beta = 0$ case, respectively. Curve 1 practically coincides with the thick line in figure 1 and the magnetic surfaces for the $\beta = 0$ case practically coincide with the magnetic surfaces of the vacuum magnetic field for the region inside the thick lines of figure 1. For the $\langle\beta\rangle = 1\%$ case, the outermost magnetic surface (curve 2 in figure 2) has a somewhat smaller size than for the $\beta = 0$ case. The magnetic surfaces for the $\langle\beta\rangle = 1\%$ case are shifted to the outside of the torus. Note that the outermost magnetic surfaces obtained with the PIES code differ a little from the initial boundary surface for the free-boundary run (curve 5 in figure 2). It is also interesting to note that the outer parts of all three surfaces coincide at about 6.2 m as can be seen from figure 2.

3. Effective ripple and $1/\nu$ neoclassical transport

It is well-known that for the $1/\nu$ transport regime the characteristic features of the specific magnetic field geometry manifest themselves in particle and heat fluxes, through the factor $\epsilon_{\text{eff}}^{3/2}$, where ϵ_{eff} is the so-called effective ripple. For the conventional stellarator field ϵ_{eff} coincides with the helical ripple ϵ_{h} (see, e.g. [10]). For an arbitrary stellarator magnetic field, in accordance with [5], the quantity $\epsilon_{\text{eff}}^{3/2}$ can be calculated with the help of the following expression:

$$\epsilon_{\text{eff}}^{3/2} = \frac{\pi R_0^2}{8\sqrt{2}} \lim_{L_s \rightarrow \infty} \left(\int_0^{L_s} \frac{ds}{B} \right) \left(\int_0^{L_s} \frac{ds}{B} |\nabla\psi| \right)^{-2} \int_{B_{\text{min}}^{\text{abs}}/B_0}^{B_{\text{max}}^{\text{abs}}/B_0} db' \sum_{j=1}^{j_{\text{max}}} \frac{\hat{H}_j^2}{\hat{I}_j}, \quad (6)$$

$$\hat{H}_j = \frac{1}{b'} \int_{s_j^{\text{min}}}^{s_j^{\text{max}}} \frac{ds}{B} \sqrt{b' - \frac{B}{B_0}} \left(4 \frac{B_0}{B} - \frac{1}{b'} \right) |\nabla\psi| k_G, \quad \hat{I}_j = \int_{s_j^{\text{min}}}^{s_j^{\text{max}}} \frac{ds}{B} \sqrt{1 - \frac{B}{B_0 b'}}. \quad (7)$$

Here, R_0 is the major radius of the torus, B_0 is a reference magnetic field, ψ the label of the magnetic surface and $k_G = (\mathbf{h} \times (\mathbf{h} \cdot \nabla)\mathbf{h}) \cdot \nabla\psi / |\nabla\psi|$ is the geodesic curvature of a magnetic field line with the unit vector $\mathbf{h} = \mathbf{B}/B$.

The quantity ϵ_{eff} is calculated by integration along the magnetic field line length, s , over a sufficiently large interval $0-L_s$, and by integration over the perpendicular adiabatic invariant of trapped particles, J_{\perp} , by means of the variable b' . Here, $B_{\text{min}}^{\text{abs}}$ and $B_{\text{max}}^{\text{abs}}$ are the minimum and maximum values of B within the interval $0-L_s$. The quantities s_j^{min} and s_j^{max} within the sum over j in (6) and (7) correspond to the turning points of trapped particles.

Note that formulae (6) and (7) must be supplemented with the magnetic field line equations as well as with the equations for the vector $\mathbf{P} \equiv \nabla\psi$ (see [11])

$$\frac{dP_i}{ds} = -\frac{1}{B} \frac{\partial B^j}{\partial \xi^i} P_j, \quad (8)$$

where B^j are the contravariant components of \mathbf{B} in real-space coordinates ξ^i , and $P_j = \partial\psi/\partial\xi^j$ are the covariant components of \mathbf{P} .

4. Computational results for the effective ripple

The results of $\epsilon_{\text{eff}}^{3/2}$ computations are shown in figure 3. These results are presented as functions of the ratio r/a with r being the mean radius of the magnetic surface under consideration, and a being the mean radius of the outermost magnetic surface resulting from a PIES run. In the case of the magnetic field directly produced by the modular coils, the mean radius a belongs to the magnetic surface corresponding to the thick lines in figure 1. For this field, figure 3 (curve 1) shows $\epsilon_{\text{eff}}^{3/2}$ only for the region inside the thick lines in figure 1. For almost the whole region $\epsilon_{\text{eff}}^{3/2}$ is approximately within the limits 0.0025–0.0035. Only near $r/a = 1$, $\epsilon_{\text{eff}}^{3/2}$ has a sharp increase to a significantly larger value. Figure 3 does not show computational results that were obtained for the outer region in figure 1 also. From these results it follows that, in this region, $\epsilon_{\text{eff}}^{3/2}$ increases to 0.007–0.012 and reaches values commensurate to the $\epsilon_{\text{eff}}^{3/2}$ values for a conventional stellarator. Note that the sharp increase of the effective ripple near $r/a = 1$

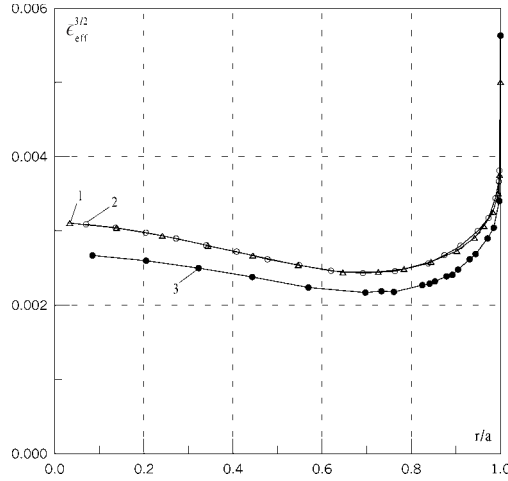


Figure 3. The parameter $\epsilon_{\text{eff}}^{3/2}$ for the magnetic field produced by modular coils (curve 1 marked by Δ) and for the fields obtained as results of PIES runs for $\beta = 0$ (curve 2 marked by \circ) and $\langle\beta\rangle = 1\%$ (curve 3).

can be explained by the behaviour of $\langle |\nabla\psi| \rangle$ (the angular brackets $\langle \rangle$ denote the flux surface average defined by (10); see the next section). From the $\langle |\nabla\psi| \rangle$ computations it follows that for the $\langle \beta \rangle = 1\%$ case the increase of $\epsilon_{\text{eff}}^{3/2}$ from 3×10^{-3} to 5.6×10^{-3} (see figure 3) correlates with the decrease of $\langle |\nabla\psi| \rangle$ from 0.4 to 0.25 (with $|\nabla\psi| = 1$ being the starting $|\nabla\psi|$ value on the outer side of the magnetic surface for $z = 0$ and $\varphi = 0$).

From figure 3 it follows that for the magnetic field from the PIES code in the zero β case, $\epsilon_{\text{eff}}^{3/2}$ practically coincides with $\epsilon_{\text{eff}}^{3/2}$ for the field produced by the modular coils (for the corresponding region). For the $\langle \beta \rangle = 1\%$ case, $\epsilon_{\text{eff}}^{3/2}$ turns out to be somewhat smaller than for the zero β case.

For a conventional stellarator with equivalent sizes, the $\epsilon_{\text{eff}}^{3/2}$ value is within the limits 0.01–0.03. For significant parts of the magnetic configurations, PIES equilibria result in values for $\epsilon_{\text{eff}}^{3/2}$ that are within the limits 0.0022–0.0035. These values are essentially smaller than those for a conventional stellarator. However, it should be noted that they are approximately two times larger than the corresponding values of $\epsilon_{\text{eff}}^{3/2}$ that were previously found for the ideal W7-X model configuration in [12]. This difference is due to the fact that the ideal configuration is the result of a configuration optimization by variation of the boundary without recourse to modular coils (using a fixed boundary equilibrium in magnetic coordinates) while, in this work, the real coil geometry is considered, particularly taking into account the influence of the 5/5 islands on the geometry.

5. Bootstrap current computation

In magnetic coordinates, bootstrap currents in the $1/\nu$ regime for stellarators were theoretically studied (e.g. [13–16]) and calculated in a number of references (e.g. [15, 17, 18]). Equations obtained in [13–16] contain geometrical factors that are convenient for the analysis of the role of the magnetic field geometry in computations of the bootstrap current for specific stellarator devices.

Analogous equations for the case of real-space coordinates were obtained in [6, 7]. In accordance with [6, 7] the geometric factor λ_b for the bootstrap current is determined as a dimensionless quantity by integration along the magnetic field line length, s , for the magnetic surface under consideration, and is given by the following formulae:

$$\lambda_b = \frac{\langle \lambda_{\text{PS}} B^2 \rangle}{\langle B^2 \rangle} + \lambda_B \quad (9)$$

with

$$\langle A \rangle = \lim_{L \rightarrow \infty} \left(\int_0^L \frac{ds}{B} \right)^{-1} \int_0^L ds \frac{A}{B}, \quad (10)$$

$$\lambda_{\text{PS}}(s) = \frac{2B_0^2}{\langle |\nabla\psi| \rangle} Y_{\text{PS}}(s), \quad Y_{\text{PS}}(s) = \int_{s_m}^s ds' \frac{|\nabla\psi| k_G}{B^2}, \quad (11)$$

$$\lambda_B = \frac{3B_0^2}{8\langle |\nabla\psi| \rangle} \lim_{L \rightarrow \infty} \frac{1}{v^3} \int_0^{J_{\perp \text{min}}^{\text{abs}}} dJ_{\perp} J_{\perp}^2 \frac{1}{I_L} \int_{s_m}^L ds \frac{|v_{\parallel}|}{B} Y_B(s), \quad (12)$$

$$Y_B(s) = \int_{s_m}^s ds' \frac{B |\nabla\psi| k_G}{|v_{\parallel}|^3}, \quad I_L = \int_{s_m}^L ds \frac{|v_{\parallel}|}{B}, \quad (13)$$

where $v_{\parallel}^2 = v^2 - J_{\perp} B$, $J_{\perp} = v_{\perp}^2/B$, $J_{\perp \text{min}}^{\text{abs}} = v^2/B_{\text{max}}^{\text{abs}}$ corresponds to the trapped-passing boundary, $B_{\text{max}}^{\text{abs}}$ is the global maximum of B on the particular magnetic field line, and s_m is the position of this maximum. All other notation is the same as that used in (6) and (7).

Again, the advantage of these expressions is that for magnetic fields originally available in real-space coordinates, calculations can be performed without a field transformation to magnetic coordinates. At the same time, these equations allow one to carry out computations in magnetic coordinates also. In this case, since λ_b is a dimensionless quantity and ψ is an arbitrary magnetic surface label, an arbitrary magnetic coordinate system can be used. Making a transformation to Hamada and Boozer coordinates, one can find that the $\lambda_b \langle B^2 \rangle / B_0^2$ quantity can be written as the quantity $f_t \langle G_{BS} \rangle_a / \langle |\nabla V| \rangle$ of [16] or the quantity $f_t G_{bs} / \langle |\nabla \psi| \rangle$ of [17], respectively, where $\langle G_{BS} \rangle_a$ was obtained using the results of [13], f_t is the fraction of trapped particles and V is the volume enclosed by the magnetic surface under consideration. In the case of a transformation to Boozer coordinates, it turns out that the λ_b factor is close to the corresponding factor in [14].

Calculations of λ_b for a number of stellarator magnetic configurations are made in [6,7,19] in real-space coordinates as well as in Boozer magnetic coordinates. From these calculations it follows, in particular, that computational results obtained for a large aspect ratio tokamak are in very good agreement with results given by analytical theory for a tokamak, and that for the W7-X vacuum magnetic field corresponding to a fixed boundary equilibrium the geometrical factor is essentially smaller than those for stellarators of different type as well as for an equivalent tokamak.

Here, the calculations of λ_b are performed for the W7-X vacuum magnetic field produced by modular coils as well as for the magnetic field from the PIES code for $\langle \beta \rangle = 1\%$, in both cases for non-resonant magnetic surfaces.

The results of the λ_b computation are shown in figures 4 and 5 (curve 1) as functions of the r/a ratio. Almost for the whole interval of r/a values, λ_b is negative and changes its sign only very near the edge of the configurations. Here, the rotational transform ι has an anti-clockwise direction with increasing toroidal angle. Therefore, for a negative λ_b the sign of the bootstrap current is such that it increases the rotational transform.

For comparison, the corresponding results for the case of a finite β equilibrium with a fixed boundary with Boozer data sets from [12] are also shown in figures 4 and 5 by curve 2. This curve is very close to the analogous curves in [6, 19] for the W7-X vacuum magnetic

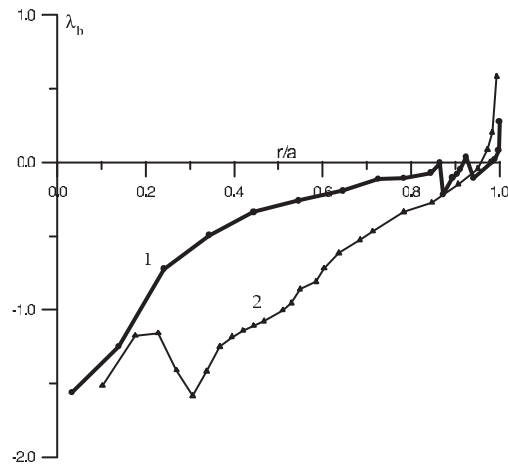


Figure 4. The parameter λ_b for the magnetic field produced by the modular coils (curve 1) and for the Boozer data corresponding to a finite β equilibrium with a fixed boundary (curve 2 marked by Δ).

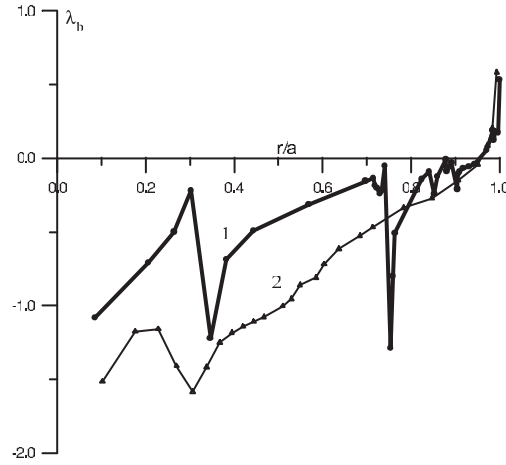


Figure 5. Same as figure 4 for the field obtained as a result of a PIES run for $\langle\beta\rangle = 1\%$ (curve 1).

field represented in terms of toroidal harmonic functions. It follows from the analysis which was carried out in [6, 19] that over the whole r/a region the ratio of λ_b for W7-X to λ_b for an equivalent tokamak does not exceed 0.25. It should be noted that this is in accordance with the results of [9], where the bootstrap current for W7-X was investigated with global Monte Carlo simulation as well as with the DKES code, and where well converged results for the bootstrap current were obtained using the DKES code.

From figures 4 and 5 we can conclude that the absolute values of λ_b for the magnetic field from the modular coils and from the PIES code are smaller than the absolute values obtained for the fixed-boundary case. At the same time, a rather large irregularity of λ_b is seen in the vicinity of the resonant magnetic surfaces with a rotational transform close to rational numbers. This is seen in a larger degree for the PIES data for $\langle\beta\rangle = 1\%$ for ι close to $15/17$ ($r/a \approx 0.35$), $10/11$ ($r/a \approx 0.75$), $25/27$ ($r/a \approx 0.84$) and $15/16$ ($r/a \approx 0.9$). For the vacuum field this is seen for ι close to $25/27$ ($r/a \approx 0.87$) and $20/21$ ($r/a \approx 0.94$). The observed irregularity is directly related to the bootstrap current resonances which can arise for resonant magnetic surfaces and which are especially important in the limit of low particle collision frequencies [19].

Here, the following remark has to be made. If the fraction of the trapped particles is not very small then it follows from [13] that in the expression for the bootstrap current an additional factor appears, which is approximately equal to $1/f_c$, with f_c being the fraction of circulating particles:

$$f_c = \frac{3}{4} \frac{\langle B^2 \rangle}{(B_{\max}^{\text{abs}})^2} \int_0^1 \frac{\lambda d\lambda}{\langle (1 - \lambda B/B_{\max}^{\text{abs}})^{1/2} \rangle}, \quad (14)$$

with $\lambda = J_{\perp} B_{\max}^{\text{abs}} / v^2$.

So, in general, this leads to an increase in the values of the general geometrical factor in comparison with the λ_b value. Figure 6 shows the plots of this additional factor for the magnetic field considered, in real-space coordinates. It turns out that this factor increases approximately from 1.8 in the centre to 2.5 at the edge of the configurations.

The analogous increase also takes place for an equivalent tokamak. For example, for $r/R_0 = 0.01, 0.02, 0.04, 0.1, 0.15$ and 0.2 the $1/f_c$ value turns out to be 1.171, 1.26, 1.412, 1.86, 2.3 and 2.88, respectively.

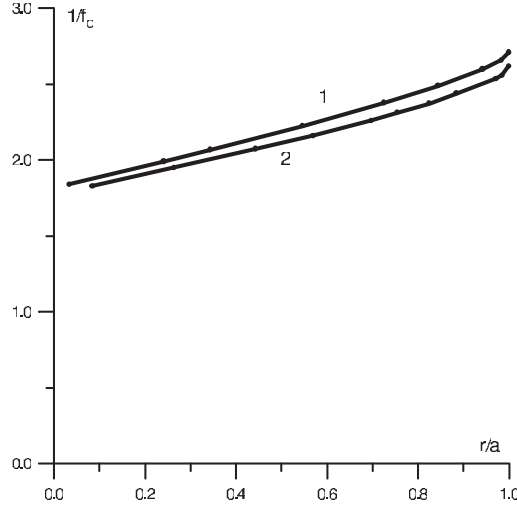


Figure 6. The parameter $1/f_c$ for the magnetic field produced by modular coils (curve 1) and for the field obtained as a result of a PIES run for $\langle\beta\rangle = 1\%$ (curve 2).

Note, that formula (14) was obtained in [13] and was used in [16–18]. A somewhat similar formula was also obtained in [14]. In these papers, the definition $f_t = 1 - f_c$ is used for the fraction of trapped particles, f_t . It should also be noted that when f_t/f_c is not small the additional factor in the bootstrap current becomes more complicated. In this case, terms of order $1/f_c$ and f_t/f_c^2 take part in its formation (see [15–17]).

6. Variation of J on a magnetic surface

A useful part of the analysis of stellarator confinement properties is connected with the investigation of the second adiabatic invariant $J = \oint v_{\parallel} dl$, in particular the investigation of the variation of J on a magnetic surface. This variation is proportional to the bounce-averaged drift of trapped particles across the magnetic surface.

Here, this variation is studied for the case of PIES data for $\langle\beta\rangle = 1\%$. The method derived in [20] is used for this purpose, which is based on integration along the magnetic field lines. The computational results for the variation of J can be presented in a normalized form as a functional dependence between the dimensionless parameters η and γ with

$$\eta = \frac{R_0}{J_{\perp} B} \frac{\omega_c}{\tau_b} \frac{\delta\psi}{\langle|\nabla\psi|\rangle}, \quad (15)$$

$$\gamma = \frac{v_{\parallel i}}{v_{\perp 0}}. \quad (16)$$

Here, τ_b is the bounce time, $\delta\psi$ is the differential of ψ during τ_b , $v_{\perp 0} = \sqrt{J_{\perp} B_0}$ and $\omega_c = eB/(mc)$ is the cyclotron frequency. The quantity $v_{\parallel i}$ is the parallel velocity v_{\parallel} at the point of a local minimum of B for which the η parameter is calculated. The γ parameter is related to the pitch angle at the point of the local minimum of B or, accordingly, to the depth of particle trapping. The normalization of η is performed in such a way that for the conventional stellarator magnetic field [10], the result is $\eta = \eta_m \sin \vartheta$, where ϑ is the poloidal angle in quasi-toroidal coordinates and $\eta_m = 0.5$.

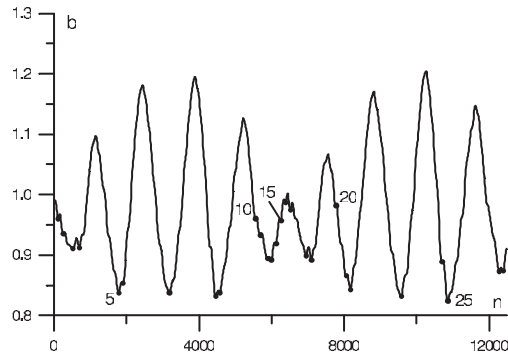


Figure 7. Distribution of $b = B/B_0$ along the magnetic field line for the magnetic surface with $r/a = 0.985$; n is the number of integration steps with 1280 steps per magnetic field period.

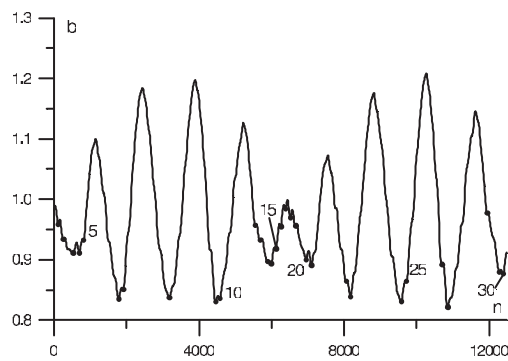


Figure 8. Same as figure 7 for the outermost magnetic surface.

Calculations of η are made for two magnetic surfaces, namely for the surface corresponding to $r/a = 0.985$ for which $\epsilon_{\text{eff}}^{3/2}$ is approximately 3×10^{-3} and for the outermost surface with a rather large effective ripple (see figure 3).

For these magnetic surfaces, figures 7 and 8 show the values of $b = B/B_0$ along magnetic field lines over the range of 27 and 30 local minima of B . Every fifth of these minima is marked by the corresponding number. Together with the minima of B corresponding to helical and mirror fields, many relatively small ripples of B corresponding to discrete coils are also seen. For the outermost magnetic surface, the fraction of these discrete ripples is only slightly larger than for the surface with $r/a = 0.985$.

A number of characteristic results for η are presented in figures 9 and 10 as functions of γ . The curves are numbered in accordance with the numbering of the minima of B in figures 7 and 8. These curves show η values for γ intervals which correspond to the pitch angles of trapped particles. For these curves the sharp change of η marks the transition from γ corresponding to particles being trapped within one ripple well to γ corresponding to particles being trapped within a few ripple wells. For some minima of B , only those η which correspond to particles being trapped within one ripple well are shown, to avoid overloading of the figures. The rather small η values for larger γ values are omitted in these cases.

It follows from the results that for some minima of B the maximum values of η , η_m , are approximately 1.5 times larger (for $r/a = 0.985$), and even two times bigger (for the outermost surface), than that for the conventional stellarator ($\eta_m = 0.5$). However, the fraction of

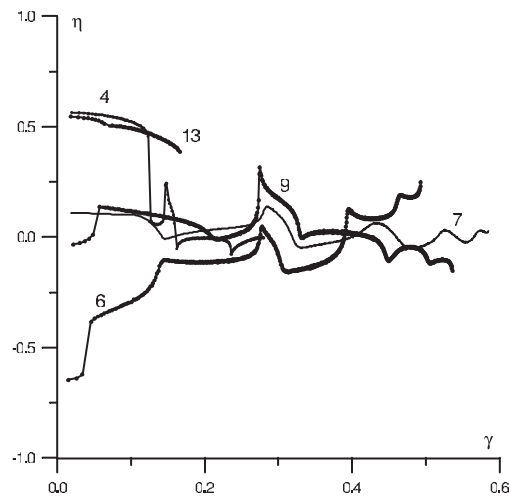


Figure 9. The parameter η as a function of γ for the magnetic surface with $r/a = 0.985$ for various local minima of B .

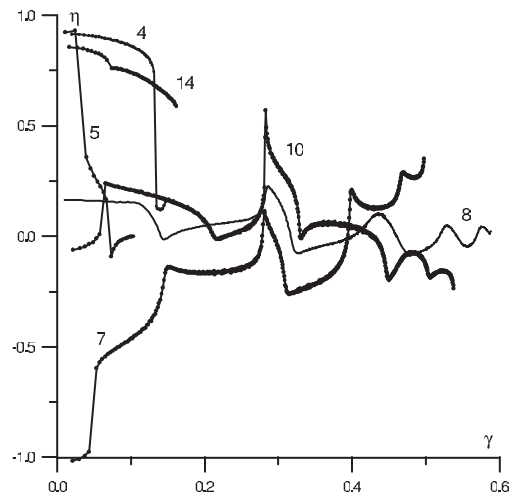


Figure 10. Same as figure 9 for the outermost magnetic surface.

trapped particles of such a kind is rather small because the corresponding γ intervals are rather limited.

It is necessary to note that except for one case the results are shown for the same minima of B for both magnetic surfaces. With respect to figures 7 and 9, in figure 10 the numbers of minima for the outermost surface are shifted by one starting from number 6. The reason is the absence of a minimum of B between the points 4 and 5 in figure 7. The corresponding minimum appears in figure 8. As a result an additional curve 5, is present in figure 10.

Comparing the plots in figures 9 and 10, one can conclude that the corresponding curves have the same characteristics in both figures. However, for the outermost magnetic surface for all trapped particles, the η values are approximately 1.5 times larger in magnitude than those for the magnetic surface with $r/a = 0.985$.

Therefore, one can conclude that this increase in η for all trapped particles is the main reason for the increased effective ripple for the outermost magnetic surface, which was found in section 4.

7. Conclusions

In this paper, confinement regions of the W7-X magnetic field obtained as results of free-boundary PIES runs for zero β as well as for $\langle\beta\rangle = 1\%$ are studied. This is the first time that neoclassical properties are evaluated, in particular near a finite-beta three-dimensional separatrix calculated using first principles equilibrium code, which should give more reliable results than the hitherto standardly used NEMEC code [21].

For almost the whole region, the values of the $\epsilon_{\text{eff}}^{3/2}$ parameter turn out to be within the limits 0.0022–0.0035. This gives ϵ_{eff} values in the range from 1.7% to 2.3%. For the $\langle\beta\rangle = 1\%$ case, $\epsilon_{\text{eff}}^{3/2}$ is found to be somewhat smaller than for the zero β case. The $\epsilon_{\text{eff}}^{3/2}$ values obtained are essentially smaller than those for a conventional stellarator of equivalent size although they are approximately two times bigger than the corresponding values obtained in [12] for the ideal W7-X model configuration, which is the result of configuration optimization without taking into account the real coil geometry. Only in the close vicinity of the outermost magnetic surfaces a rather large sharp increase in $\epsilon_{\text{eff}}^{3/2}$ takes place. This sharp increase correlates with the corresponding decrease in the $\langle|\nabla\psi|\rangle^2$ value.

The results for the zero β case are in very good agreement with the corresponding results for the vacuum magnetic field produced by modular coils of the device. This takes place for the region inside the magnetic surface corresponding to the outermost magnetic surface for the PIES run. For the vacuum configuration, in the region outside this magnetic surface the $\epsilon_{\text{eff}}^{3/2}$ values become essentially larger.

So, one finds larger $\epsilon_{\text{eff}}^{3/2}$ values compared to $\epsilon_{\text{eff}}^{3/2}$ values for the ideal W7-X model configuration as well as increased $\epsilon_{\text{eff}}^{3/2}$ values in the vicinity of the outermost magnetic surfaces and in the outer region of the vacuum configuration (see figure 1). All these facts result from differences in the magnetic field geometry.

It follows from the computation of the geometrical factor λ_b for the bootstrap current that this factor does not exceed the values found earlier for the ideal W7-X model configuration. However, the irregularity of λ_b in the vicinity of the resonant magnetic surfaces for the $\langle\beta\rangle = 1\%$ case is larger than that for the vacuum magnetic field produced by modular coils.

The analysis of the variation of the second adiabatic invariant, J , on the magnetic surface for the $\langle\beta\rangle = 1\%$ case is carried out for the outermost magnetic surface and for an inner surface rather close to the outermost one. It is found that the fractions of relatively small ripples of B corresponding to discrete coils are similar for both surfaces and fractions of particles trapped in these ripples are smaller when compared to the fractions of particles trapped within the main ripples.

The normalized variation of J (velocity of the bounce-averaged drift) for the outermost magnetic surface turns out to be larger than that for the inner surface. This is in good agreement with the results of effective ripple computations. The resulting increase takes place both for particles being trapped within the small discrete ripples and for particles being trapped within the main ripples that form the major part of the trapped particle population. Therefore, one can conclude that the increased effective ripple for the outermost magnetic surface as compared to the inner surface is a result of increased bounce-averaged drift for all trapped particles but not a result of discrete ripples of B resulting from discrete coils.

Acknowledgments

This work was partly supported by the project INTAS-99-00592, by the Austrian Academy of Sciences and by the Association of EURATOM with the Austrian Academy of Sciences. The content of the publication is the sole responsibility of its publishers and it does not necessarily represent the views of the Commission or its services.

References

- [1] Reiman A H and Greenside H 1988 *J. Comput. Phys.* **75** 423
- [2] Reiman A *et al* 2001 *Phys. Plasmas* **8** 2083
- [3] Grieger G *et al* 1991 *Plasma Physics and Controlled Nuclear Fusion Research 1990* vol 3 (Vienna: IAEA) p 525
- [4] Grieger G *et al* 1992 *Phys. Fluids B* **4** 2081
- [5] Nemov V V, Kasilov S V, Kernbichler W and Heyn M F 1999 *Phys. Plasmas* **6** 4622
- [6] Kasilov S V, Nemov V V, Kernbichler W and Heyn M F 2000 *27th EPS Conf. Controlled Fusion and Plasma Physics (Budapest, Hungary, 12–16 June 2000)* ed K Szego *et al Report* P2.066
- [7] Kernbichler W, Nemov V V, Kasilov S V and Heyn M F 2000 Problems of atomic science and technology series *Plasma Phys.* 6
- [8] Nührenberg J and Zille R 1986 *Phys. Lett. A* **114** 129
- [9] Maassberg H, Lotz W and Nührenberg J 1993 *Phys. Fluids B* **5** 3728
- [10] Galeev A A and Sagdeev R Z 1979 *Reviews of Plasma Physics* vol 7, ed M A Leontovich (New York: Consultants Bureau) p 257 [see also in *Voprosy Teorii Plazmy* vol 7 (Moscow: Atomizdat) p 205 (in Russian)]
- [11] Nemov V V 1988 *Nucl. Fusion* **28** 1727
- [12] Nemov V V, Kasilov S V, Nührenberg C, Nührenberg J, Kernbichler W and Heyn M F 2003 *Plasma Phys. Control. Fusion* **45** 43
- [13] Shaing K C and Callen J D 1983 *Phys. Fluids* **26** 3315
- [14] Boozer A H and Gardner H J 1990 *Phys. Fluids B* **2** 2408
- [15] Shaing K C, Carreras B A, Dominguez N, Lynch V E and Tolliver J S 1989 *Phys. Fluids B* **1** 1663
- [16] Nakajima N and Okamoto M 1992 *J. Phys. Soc. Japan* **61** 833
- [17] Watanabe K, Nakajima N, Okamoto M, Nakamura Y and Wakatani M 1992 *Nucl. Fusion* **32** 1499
- [18] Johnson J L, Ichiguchi K, Nakamura Y, Okamoto M, Wakatani M and Nakajima N 1999 *Phys. Plasmas* **6** 2513
- [19] Kernbichler W, Kasilov S V, Nemov V V, Leitold C and Heyn M F 2002 *29th EPS Conf. on Plasma Physics and Controlled Fusion (Montreux, Switzerland, 17–21 June 2002)* vol 26B (ECA) P2.100
- [20] Nemov V V 1999 *Phys. Plasmas* **6** 122
- [21] Hirshman S P, Van Rij W I and Merkel P 1986 *Comput. Phys. Commun.* **43** 143